



## Atmospheric and surface retrievals in the Mars polar regions from the Thermal Emission Spectrometer measurements

Janusz Eluszkiewicz,<sup>1</sup> Jean-Luc Moncet,<sup>1</sup> Mark W. Shephard,<sup>1</sup> Karen Cady-Pereira,<sup>1</sup> Thomas Connor,<sup>1</sup> and Gennady Uymin<sup>1</sup>

Received 26 February 2008; revised 12 June 2008; accepted 31 July 2008; published 31 October 2008.

[1] Retrievals of atmospheric temperatures, surface emissivities, and dust opacities in the Mars polar regions from the Thermal Emission Spectrometer (TES) spectra are presented. The retrievals correspond to two types of spectra, characterized by small and large band depths  $BD_{25}$  in the 25- $\mu\text{m}$  band of solid  $\text{CO}_2$ . These two types of spectra have previously been identified with locations covered by slab ice and fluffy  $\text{CO}_2$  frost, respectively. Above the first atmospheric scale height, there is a correlation between the degree of saturation in the retrieved atmospheric temperatures and the two types of surface, with the high  $BD_{25}$  spectra (“cold spots”) showing larger supersaturations around 1 mbar. This supports the hypothesis that cold spots correspond to locations with potential or actual atmospheric precipitation. Furthermore, the retrieved temperature profiles exhibit a warming above 1 mbar (15 km), which appears real even when the limited number of independent pieces of information from the measurement ( $\sim 3$ ) and coarse vertical resolution of the TES instrument above 15 km are considered. The spectral shape of the retrieved surface emissivities in the cold spot locations is consistent with modeling results attributing high  $BD_{25}$  to porosity. For the low  $BD_{25}$  spectra, the retrieved emissivities are spectrally flat but significantly less than unity (0.8–0.9). The cause of these spectrally uniform deviations from blackbody behavior (which are not supported by modeling) remains to be investigated, with a noticeable reduction in the deviation from the blackbody behavior achieved through a zero-radiance-level correction to the TES spectra available from the Planetary Data System.

**Citation:** Eluszkiewicz, J., J.-L. Moncet, M. W. Shephard, K. Cady-Pereira, T. Connor, and G. Uymin (2008), Atmospheric and surface retrievals in the Mars polar regions from the Thermal Emission Spectrometer measurements, *J. Geophys. Res.*, *113*, E10010, doi:10.1029/2008JE003120.

### 1. Introduction

[2] The Thermal Emission Spectrometer (TES) aboard the Mars Global Surveyor (MGS) spacecraft has generated an unprecedented wealth of information about Mars. Although TES is primarily a surface-oriented instrument [Christensen *et al.*, 2001], analyses of TES spectra have also yielded abundant information about the Martian atmosphere, including its thermal structure, dust and water ice opacity, column abundance of water vapor, and optical properties of airborne dust and water ice particles [Conrath *et al.*, 2000; Smith *et al.*, 2000; Smith, 2002; Wolff and Clancy, 2003]. The information about the spatial and temporal variability in these parameters has in turn enabled a wide range of scientific studies. In particular, TES retrievals have led to a description of the amplitudes, dominant wave periods, and seasonal evolution of planetary waves [Wilson, 2000; Wilson *et al.*, 2002; Banfield *et al.*, 2003, 2004; Wang *et al.*, 2005], provided insights into dust storm generation mechanisms [Wang *et al.*, 2003], and,

together with the Viking data, have served as a reference to studies of the Mars water cycle [Richardson and Wilson, 2002].

[3] The focus of the TES retrieval work to date has been on the nonpolar regions. For example, the opacity product in the Planetary Data System (PDS) is essentially nonexistent when the surface temperature drops below about 220 K. This is principally due to the small thermal contrast between the atmosphere and the surface, particularly in situations when the surface has near-blackbody emissivities [Smith, 2004]. Furthermore, the polar temperature profiles in the PDS have been obtained without specifically accounting for the polar surface emissivities that are often very different from the nonpolar emissivities. This affects both the convergence rate of the retrievals as well as accuracy of the retrieved atmospheric temperatures in the near-surface layer. In this paper, we present initial results from simultaneous retrievals of atmospheric and surface parameters from the TES polar spectra using an inversion algorithm adapted to Mars from our terrestrial remote sensing applications [Moncet *et al.*, 2001]. Two factors critical to the success of our retrievals are as follows:

[4] 1. The thermal contrast is enhanced when the emissivity is low. Consequently, locations of anomalously low

<sup>1</sup>Atmospheric and Environmental Research, Inc., Lexington, Massachusetts, USA.

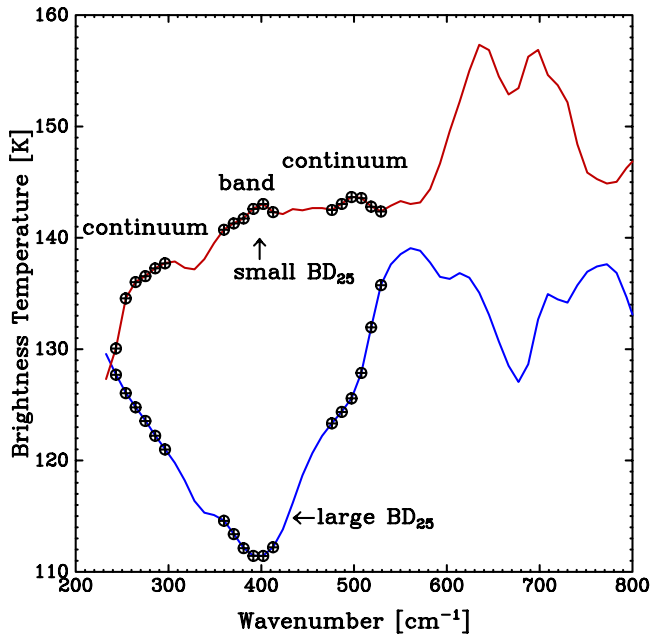


**Figure 1.** Examples of TES spectra of the southern polar cap. Circles mark spectral locations of channels used to define the 25- $\mu\text{m}$  band (the band itself and two continua). The blue spectrum has low brightness temperatures in the 25- $\mu\text{m}$  band and corresponds to a highly porous deposit. The red spectrum, with a small  $\text{BD}_{25}$ , corresponds to slab ice. Figure from *Eluszkiewicz et al.* [2005a] with permission from Elsevier.

emissivities (“cold spots”) may be the preferred locations for retrievals of atmospheric dust opacities.

[5] 2. Cold spots have been identified in the TES spectra of the polar regions [Titus *et al.*, 2001; Eluszkiewicz *et al.*, 2005a]. These locations form one of the foci of the retrieval work presented herein.

[6] While cold spots form a small subset of the total number of polar spectra, they are attributed to interesting atmospheric phenomena, e.g.,  $\text{CO}_2$  snowfall, and thus retrieving atmospheric temperature and dust opacities (as well as better constraining the surface emissivities) is likely to shed light on their formation mechanism(s). Furthermore, given the prominent role the polar caps play in the Mars global atmospheric circulation, any additional insights into their surface and the surrounding atmosphere will be important in global modeling studies.

[7] The organization of this paper is as follows. The TES data are described in section 2, followed by representative retrieval results in section 3. Section 4 offers a summary. The retrieval results presented in this paper have been obtained using a novel, in the Mars context, retrieval method adapted from our terrestrial remote sensing work. A somewhat detailed description of this method is provided in Appendix A, as it will be of interest to the Mars remote sensing community.

## 2. TES Data

[8] The primary TES data utilized in this study are the calibrated thermal IR radiance spectra available from the PDS [Christensen *et al.*, 2001; Christensen, 2002]. Specif-

ically, we use  $10\text{ cm}^{-1}$  radiances from the TES detector 1, restricting ourselves to the wave number range  $222\text{--}900\text{ cm}^{-1}$  (i.e., excluding the first five TES channels, due to obvious instrumental artifacts, and the shorter wavelength channels that have low signal-to-noise ratios at the cold polar temperatures). The zero-radiance level of the spectra available from the PDS has been corrected using software (provided by J. Bandfield and T. Titus, personal communication, 2008) that accounts for an error caused by variations of instrument radiance within the field of view with changing mirror-pointing angle [Christensen *et al.*, 2001; Kieffer *et al.*, 2000]. This correction has led to more physical results for the surface emissivity (see section 3). The surface pressure for each measurement location is taken from the PDS (these values are based on GCM simulations). In addition, atmospheric temperature profiles available from the PDS are used, primarily for validation and comparison purposes. In this preliminary study, we do not attempt a systematic processing of the large volume of the TES data. Instead, we present representative examples suggestive of significant physical interplay between atmospheric temperatures and surface emissivities.

[9] The present analysis of the TES spectra focuses on the Mars polar regions covered with the seasonal  $\text{CO}_2$  frost. Eluszkiewicz [1993] predicted the presence of both nonporous (slab-like)  $\text{CO}_2$  ice and more porous, fluffy frost, a prediction confirmed by subsequent analyses [Kieffer *et al.*, 2000; Titus *et al.*, 2001] (for completeness, we note that according to Langevin *et al.* [2006], dust coating can also mimic the slab ice behavior). A fluffy texture can be distinguished from a slab layer by the shape of the 25- $\mu\text{m}$  band of solid  $\text{CO}_2$  [Hansen, 1997] seen in the TES spectra, with large band depth  $\text{BD}_{25}$  indicative of high porosity.  $\text{BD}_{25}$  is defined as the fractional drop in the measured band radiance relative to the expected blackbody radiance at the brightness temperature of adjacent continua [Kieffer *et al.*, 2000]

$$\text{BD}_{25} = 1 - \frac{\sum R_b}{\sum B(T_c, \{\nu_b\})} \quad (1)$$

where  $R_b$  and  $\{\nu_b\}$  are the radiances and central frequencies of TES channels defining the band,  $B$  is the Planck function, and  $T_c \equiv B^{-1}(\sum R_c, \{\nu_c\})$  is the brightness temperature of the continua (where  $R_c$  and  $\{\nu_c\}$  are the radiances and central frequencies of channels defining the continua). Two sample TES spectra of the southern seasonal cap with small and large  $\text{BD}_{25}$  are shown in Figure 1.

[10] A particularly well-suited location for our analysis is the polar rings corresponding to the northernmost and southernmost latitudes of the MGS orbit ( $\pm 87^\circ$ ) that are characterized by almost daily repeat coverage. As discussed by Eluszkiewicz *et al.* [2005a], both rings are covered by slab ice (small  $\text{BD}_{25}$ ) during prolonged periods in fall and winter, while large values of  $\text{BD}_{25}$  (i.e., cold spots) occur sporadically and are best explained by the porous structure of the frost. The time scale for the disappearance of cold spots is typically short, on the order of several sols.

## 3. Results

[11] This pilot study confines itself to the retrievals on a small representative set of TES polar spectra. Specifically,

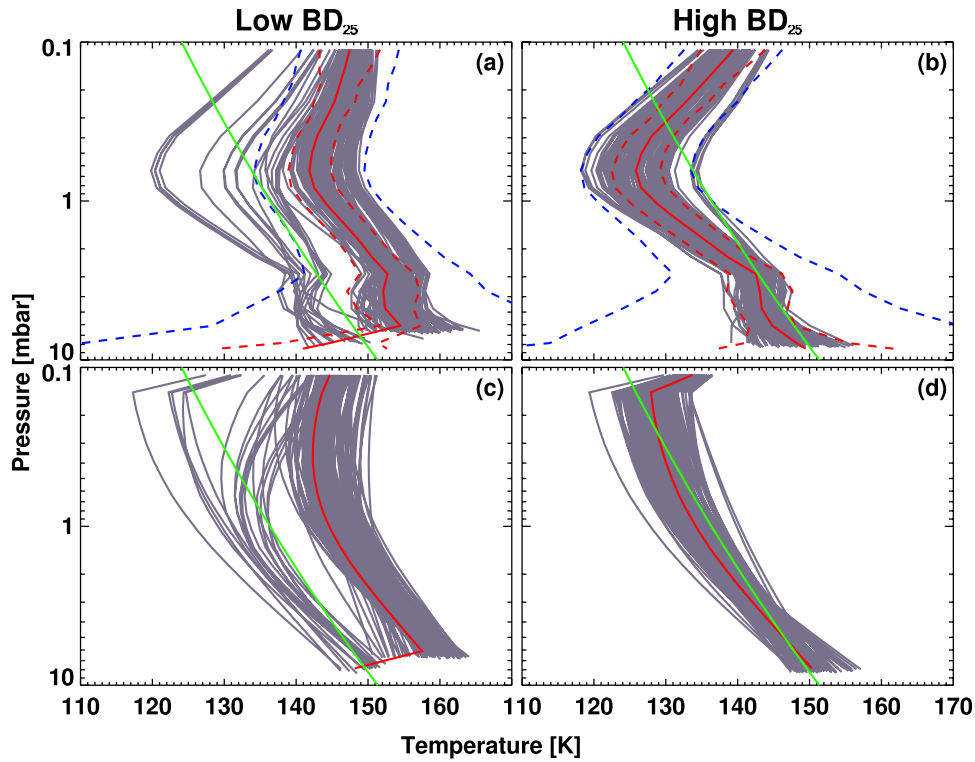


**Figure 2.** (a and b) Atmospheric temperature profiles retrieved using the algorithm described in this paper for the low and high  $BD_{25}$  spectra. (c and d) Their counterparts available from the Planetary Data System (PDS). The solid red lines represent the mean retrieved profile in each case, while the green lines represent the profile of the  $CO_2$  condensation temperature. For our profiles, the dashed blue and red lines represent a priori and a posteriori error estimates, respectively, around the mean profile (see error analysis in section 3).

we have selected 148 spectra with low  $BD_{25}$  ( $<0.05$ ) and 140 spectra with high  $BD_{25}$  ( $>0.20$ ). These spectra correspond to the northern polar ring data around  $87^\circ N$  during fall and winter analyzed by *Eluszkiewicz et al.* [2005a]. The retrieved quantities are the atmospheric temperature profiles, spectrally resolved spectral emissivities, and the optical depths of atmospheric water ice and dust. For the atmospheric particulates, we ignore scattering, instead using their spectral absorption coefficients available from the PDS [Smith, 2004] and retrieving their optical depth (i.e., the scaling factor of the PDS-provided spectral shapes). The impact of neglecting scattering is, in general, not large. For the small dust and ice optical depths we retrieve (see below), the differences between nonscattering radiances and the radiances computed using a fully scattering version of our radiative transfer code (see Appendix A1) are, on average, within the instrument noise level of 0.3 K. For some profiles, the differences do exceed the noise level, but given the isolated occurrence of this behavior, we defer the implementation of fully scattering retrievals (which are computationally much more demanding) to future work. With regard to the surface temperature  $T_{skin}$ , we essentially set it to the condensation temperature of  $CO_2$  frost  $T_{frost}$  at the assumed surface pressure. In the retrieval, this is accomplished by assigning  $T_{skin}$  to  $T_{frost}$  a priori, while allowing the retrieved  $T_{skin}$  to vary slightly (see Figure 5 below).

[12] Figures 2a and 2b show the atmospheric temperature profiles retrieved for locations characterized by near-unity emissivities and the so-called “cold spots” where the emissivities are significantly lower than unity. Since the cold spots are usually attributed to the occurrence of snowfall [Colaprete et al., 2005], it is encouraging to see that the associated temperature profiles do fall below the  $CO_2$  condensation line (plotted in green in Figure 2) more often than in the “blackbody” locations (where the  $CO_2$  frost is likely to form directly on the ground). Admittedly, the occurrence of a supersaturated region does not imply snowfall at a given time and location, but we expect that a supersaturated region is associated with snowfall nearby. The supersaturated region in Figure 2 is confined to the lowest 25 km (for an approximate altitude scale, see Figure 3 below), which is consistent with the altitude range of previous detections of  $CO_2$  clouds [Pettengill and Ford, 2000; Ivanov and Muhleman, 2001].

[13] It should be emphasized that the profiles shown in Figure 2 have been retrieved using three elements in the empirical orthogonal function (EOF) representation employed in our retrieval algorithm (see Appendix A2). This limited number of EOFs, consistent with the estimated number of the degrees of freedom (see below), only allows for retrieving the gross features of the true atmospheric profiles. In order to assess the realism of the profiles shown in Figure 2, we plot the a priori and a posteriori error

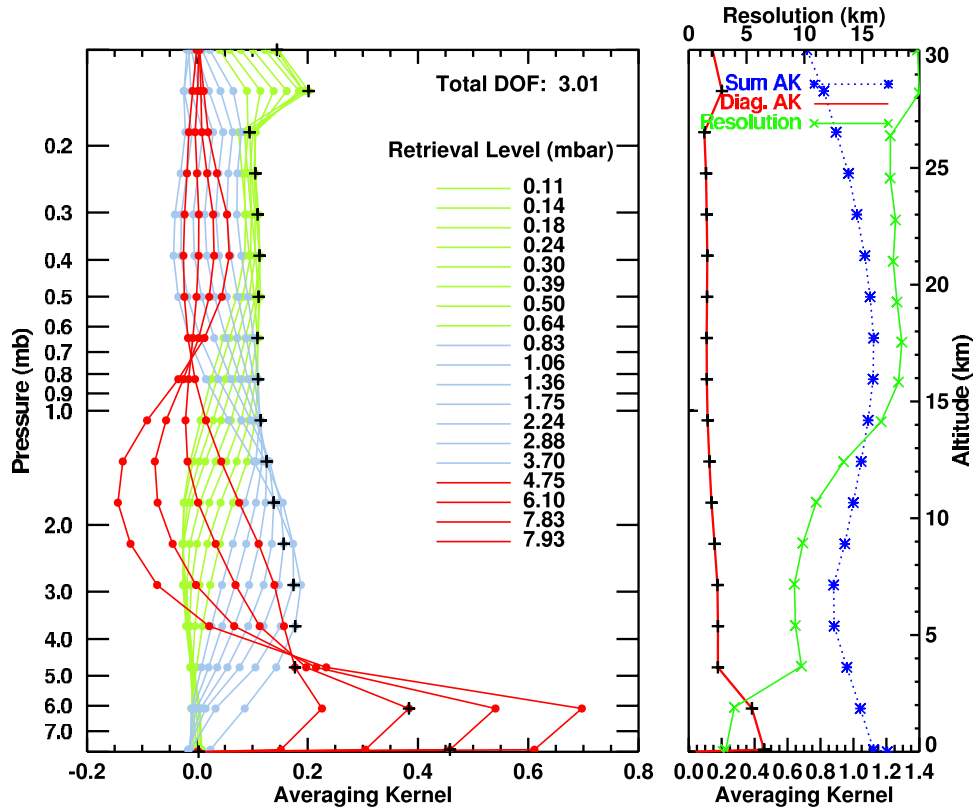


**Figure 3.** Averaging kernels for the TES retrievals described in this paper. The left shows the rows of the averaging kernel  $A$  for the individual retrieval levels (in mbar, with the surface pressure at 8.13 mbar), while the right shows the vertical profiles of the cumulative averaging kernel and its diagonal elements. Shown in green on the right is the approximate vertical resolution of the TES temperature retrieval, computed from the full width at half maximum of the rows of the averaging kernels. The reference altitude scale is shown along the right axis. The total number of degrees of freedom in the retrievals, computed as  $Tr(A)$ , is equal to about 3.

estimates, corresponding to the diagonal elements of the a priori covariance matrix  $S_{\text{prior}}$  and its a posteriori counterpart

$$S_{\text{post}} = \left( K^T S_{\varepsilon}^{-1} K + S_{\text{prior}}^{-1} \right)^{-1} \quad (2)$$

where  $S_{\varepsilon}$  is the measurement error matrix, assumed diagonal with diagonal elements equal to the TES nominal noise level (0.3 K), and  $K$  is the Jacobian matrix (derivative of channel radiance with respect to the temperature at a given retrieval level). The a priori covariance  $S_{\text{prior}}$  has been derived from a set of GCM profiles (see Appendix A). Comparing the magnitude of the a priori and a posteriori errors in Figure 2 it is clear that there is enough information in the TES radiances to reduce the a priori errors significantly. Furthermore, we have computed the averaging kernels to show the sensitivity of the retrievals,

$$A = \left( K^T S_{\varepsilon}^{-1} K + S_{\text{prior}}^{-1} \right)^{-1} K^T S_{\varepsilon}^{-1} K \quad (3)$$

The rows of  $A$  are functions of finite width that give a measure of the vertical resolution of the retrieval [Rodgers, 2000]. They are plotted in Figure 3 and are colored into three distinct altitude groups. The diagonal element of  $A$

vanishes at the level closest to the surface (surface pressure is 8.13 mbar for the profile selected for the computation shown in Figure 3), reflecting the lack of information to retrieve the atmospheric temperature at this level. The total number degrees of freedom for signal, which gives the number of independent pieces of information from the measurement, is computed as the trace of  $A$ . Provided the retrieval is relatively linear, the sum of each row of  $A$  represents the fraction of information in the retrieval that comes from the measurement rather than the a priori. The amount of available information and the vertical distribution of this information vary, depending on the atmospheric and surface conditions for upwelling radiance observations. The vertical resolution of our retrievals, defined as the half-width at half-maximum of the row of the averaging kernel (approximated as a Gaussian) at each pressure level, is plotted in green in the right panel of in Figure 3. The resolution is about 5–10 km in the lowest scale height, but degrades aloft, reaching 20 km at pressures less than 1 mbar. With such coarse resolution, it is clearly only possible to assign the broadest features to the retrieved profiles.

[14] The shape of our retrieved profiles in Figure 2 exhibits a warming between 1 and 0.1 mbar. While the reality of this shape is somewhat questionable, given the

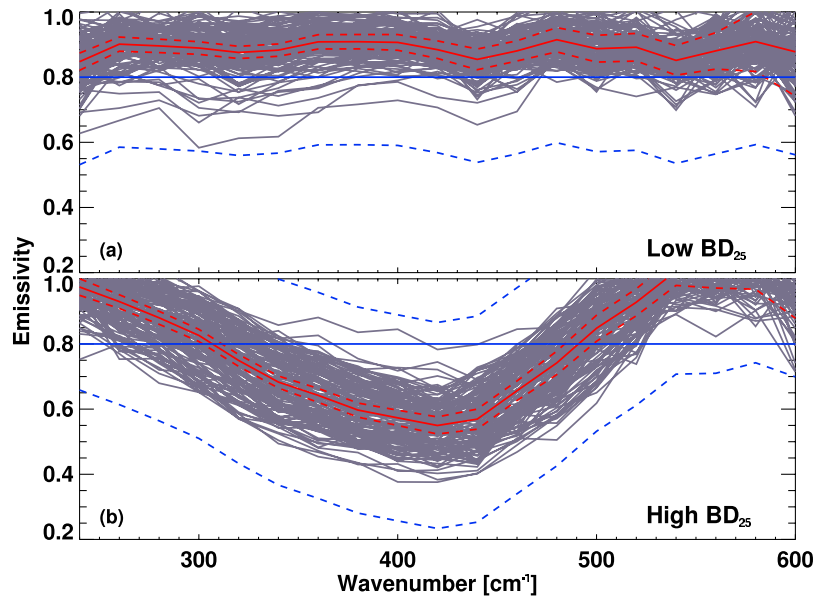


**Figure 4.** Retrieved surface emissivities. The red solid and dashed lines represent the mean retrieved emissivity and its a posteriori errors, and the blue solid and dashed lines represent the a priori emissivity and its errors.

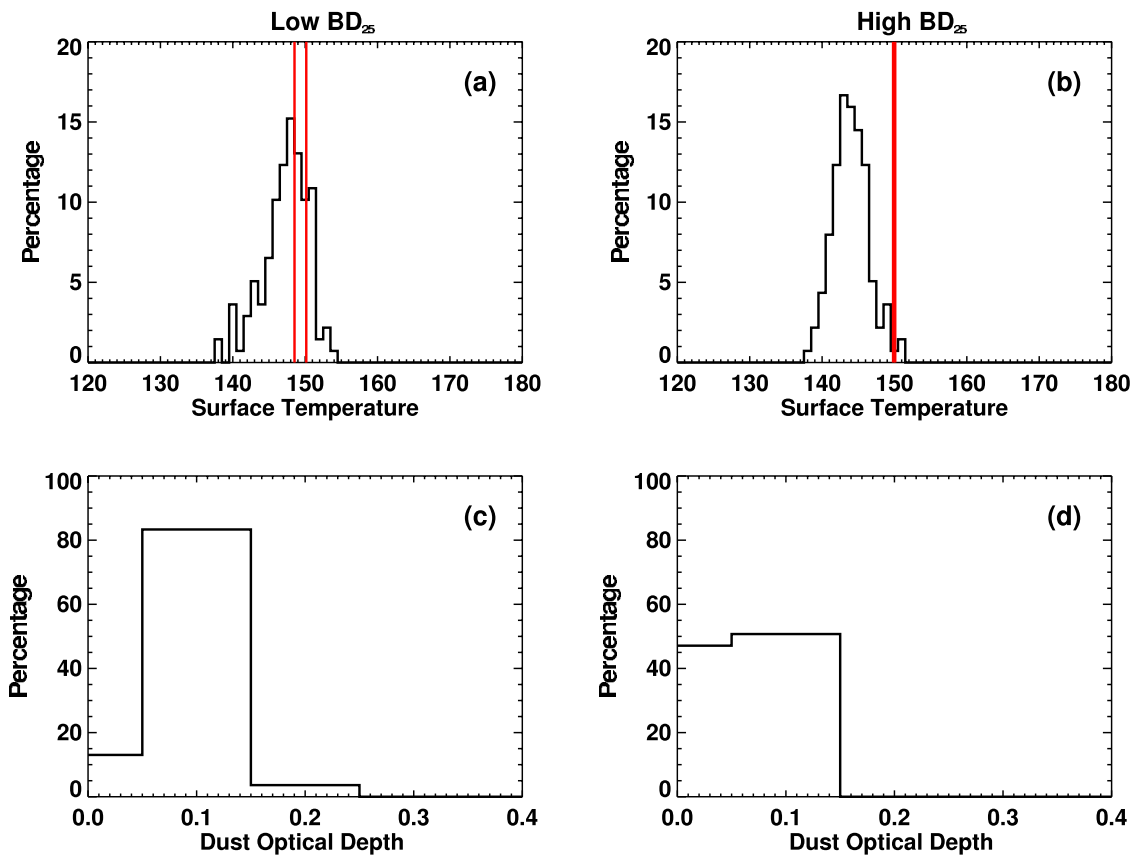


**Figure 5.** Histogram of the retrieved surface temperatures  $T_{skin}$  and dust optical depths. The red lines in Figures 5a and 5b represent the range of  $CO_2$  condensation temperatures corresponding to the surface pressures available from the PDS.

limited number of degrees of freedom and a very coarse vertical resolution above 15 km, the small a posteriori errors in this altitude region (shown as dashed red lines in Figures 2a and 2b) indicate that the warming is real. Furthermore, the qualitative aspects of the shape in our temperature profiles around 1 mbar appear consistent with results from GCM runs that take into account the interplay between cloud microphysics, convection, and large-scale dynamics [Colaprete *et al.*, 2008].

[15] For comparison, in Figures 2c and 2d we show the corresponding temperature profiles available from the PDS. The PDS profiles show the same general trend as our profiles (colder for high BD<sub>25</sub> locations), despite not considering CO<sub>2</sub> frost emissivities specifically in their surface treatment. This indicates that this aspect of both retrieval approaches is not overly sensitive to the treatment of surface emissivity. On the other hand, the PDS profiles are significantly more linear above 1 mbar, particularly in the cold spot locations.

[16] Of particular interest to the interpretation of our results are the retrieved surface emissivities, shown in Figure 4. The a priori for surface emissivities is set to a spectrally constant value of 0.8 in our retrievals (with a significantly lower or higher emissivity a priori, the retrieved  $T_{\text{skin}}$  would be significantly higher or lower than  $T_{\text{frost}}$ , respectively). As expected, for the cold spots the retrieved emissivities do deviate significantly from unity in the 25- $\mu\text{m}$  “transparency band” of solid CO<sub>2</sub> and their spectral shape is qualitatively consistent with snow emissivities modeled by Eluszkiewicz *et al.* [2005a]. In contrast, for the low BD<sub>25</sub> spectra, the retrieved emissivities are flat, but significantly less than unity (0.8–0.9), which is not supported by modeling. The cause of these spectrally uniform deviations from blackbody behavior remains to be investigated, but they might be caused by systematic errors not accounted for in our retrieval. Indeed, with the zero-radiance-level correction applied to the TES spectra (see section 2), the retrieved emissivities are brought somewhat closer to unity (by about 0.05–0.1). Even while the reasons for the remaining deviations are left for future studies, a comparison between the magnitudes of the a priori and a posteriori errors in Figure 4 reveals that there is enough information in the TES radiances to reduce the a priori errors on surface emissivity significantly. Furthermore, the estimated number of degrees of freedom is unity at each emissivity spectral point within the spectral range shown in Figure 4, underscoring the ability of the retrieval to “move away” from the a priori.

[17] Figure 5 shows the retrieved surface temperatures and dust opacities (retrieved water ice opacities are very small and are not shown here). As discussed above, the distribution of  $T_{\text{skin}}$  is centered on  $T_{\text{frost}}$  by design. The retrieved dust opacities are generally low, consistent with the “flushing” of the wintertime polar atmosphere by precipitating snow, with a hint of slightly lower opacities in the high BD<sub>25</sub> case (suggesting more active flushing in the putative snowfall locations).

#### 4. Summary

[18] The results described in this paper represent a first systematic attempt at simultaneously retrieving atmospheric and surface properties in the Mars polar regions from the

TES spectra. Clearly, such retrievals are very challenging, given the generally low signal-to-noise ratio and poor thermal contrast between the surface and the atmosphere. Nevertheless, the retrievals provide valuable insight, particularly in the cold spot locations where the thermal contrast is enhanced. Our work has demonstrated that in these locations the retrieved atmospheric temperatures tend to fall below the CO<sub>2</sub> condensation temperatures around 1 mbar, suggestive of snowfall. This behavior is already hinted at in the profiles available from the PDS, although the shape of our profiles is significantly different from their PDS counterparts above 15 km (1 mbar), even when the limited number of degrees of freedom ( $\sim 3$ ) and coarse vertical resolution ( $\sim 20$  km) above 15 km are taken into consideration. The spectral shape of the retrieved surface emissivities is realistic for the cold spot locations, with a depression in the 25- $\mu\text{m}$  band. This shape is qualitatively consistent with the modeling results by Eluszkiewicz *et al.* [2005a]. In contrast, for the low BD<sub>25</sub> spectra, the retrieved surface emissivity is spectrally flat but different from unity, which is not supported by modeling and suggests systematic errors not accounted for in our retrievals. It should be noted that the deviations from the blackbody behavior in the low BD<sub>25</sub> case have been reduced (but not eliminated) by considering a zero-radiance-level correction to the spectra available from the PDS. Within the limitations of our retrieval algorithm, in which the scattering effects of atmospheric dust are neglected, the retrieved dust optical depths are small ( $< 0.2$ ), consistent with effective flushing of the winter polar atmosphere by precipitating snow. For these small opacities, the impact of neglecting scattering is, in fact, not large, with the mean differences between scattering and nonscattering spectra within the noise level of the TES instrument.

### Appendix A: Retrieval Algorithm

#### A1. Atmospheric Forward Model

[19] The atmospheric contribution to the observed spectra is modeled using the Optimal Spectral Sampling (OSS) method [Moncet *et al.*, 2001; Eluszkiewicz *et al.*, 2005b; Saunders *et al.*, 2007]. The theoretical basis and implementation of the OSS method are described by Moncet *et al.* [2008]. The OSS approach is an extension of the Exponential Sum Fitting Transmittance (ESFT) method of Wiscombe and Evans [1977], applicable to vertically inhomogeneous atmospheres, and consists of approximating radiances in each spectral channel as linear combinations of radiances computed at selected monochromatic locations

$$R_{\Delta\nu}(\nu) = \frac{\int_{\Delta\nu} \phi(\nu - \nu') R(\nu') d\nu'}{\int_{\Delta\nu} \phi(\nu - \nu') d\nu'} = \sum_i w_i R_{\nu_i} + \varepsilon \quad (\text{A1})$$

where  $\nu_i$  belong to some spectral interval  $\Delta\nu$  around the “central” frequency  $\nu$  and  $\phi(\nu - \nu')$  is the Instrument Line Shape (ILS) function (assumed to vanish when  $\nu'$  is outside the interval  $\Delta\nu$ ). In the OSS model developed for this paper, we utilized an analytical ILS function provided by M. D. Smith (personal communication, 2005). Directly fitting radiances (rather than transmittances as in the ESFT approach) has the advantage that (1) it automatically emphasizes atmospheric levels located near the peak of

the weighting function (which contribute the most to the outgoing radiances) in the optimization process and (2) it provides a mechanism for taking into account smoothly varying functions, such as the Planck function, dust optical properties, or surface emissivity, in the determination of the model parameters.

[20] Since the OSS method is monochromatic, it is applicable to nonpositive instrument line-shape functions (interferometers) and different viewing geometries, greatly simplifies the computation of analytical Jacobians, and enables the modeling of scattering effects in an accurate and computationally efficient way (because the algorithm obeys Beer's law). While the retrievals described in this paper have been performed using the nonscattering version of OSS (thus greatly reducing the computational burden), a fully scattering version employing a version of the doubling and adding method has been used to assess the impact of the nonscattering assumption (see section 3). The OSS spectral locations and their statistical weights are selected by comparing the resulting channel radiances against line-by-line (LBL) calculations performed over a wide range of atmospheric profiles. The training profiles are chosen to be representative of the expected variability, including atmospheric temperature and composition, surface pressure, surface emissivity and reflectivity, and viewing and solar angles. In our work with OSS, the LBLRTM model [Clough *et al.*, 1992, 2005] serves as the line-by-line reference. The choice of LBLRTM gives direct access to ongoing radiance closure studies [Clough *et al.*, 1999; Turner *et al.*, 2004] and, together with the monochromatic nature of OSS, enables the OSS model to be quickly and rigorously updated as our knowledge of the fundamental spectroscopic parameters improves. A recent example involves the implementation of new P and R branch line coupling coefficients for CO<sub>2</sub> [Niro *et al.*, 2005; Clough *et al.*, 2008].

[21] Being a physical approach, the OSS method is robust with respect to the range of atmospheric conditions to which the model is applied, including profiles outside of the training set. Furthermore, the method very accurately takes into account variations in temperature and gaseous and aerosol absorption along inhomogeneous vertical paths. A distinct advantage of the method is that the error tolerance (the RMS value of  $\varepsilon$  in equation (A1)) is selected a priori by the user, even in the multilayer case. This feature provides flexibility to tailor the fitting to balance the radiometric accuracy requirements dictated by the application and the algorithm run-time constraints. Specifically, while an LBL model uses hundreds of thousands of monochromatic points to simulate a 10 cm<sup>-1</sup> channel, the OSS model relies on less than a dozen monochromatic points to achieve a specified level of accuracy. In doing so, the OSS method exploits the spectral redundancies between monochromatic lines within each channel. In other words, a few (optimally chosen) lines represent the variability of absorption in each layer of all the lines present in the channel. Examples of Mars spectra simulated with the OSS model, including errors against LBL calculations, are shown by Eluszkiewicz *et al.* [2005b].

[22] The OSS technique has been developed and extensively validated for a wide range of terrestrial applications, including retrieval algorithms for the microwave and infrared sensors. Currently, the OSS method is being considered for implementation at the National Centers for Environmen-

tal Prediction (NCEP) for operational numerical weather prediction and data assimilation [Weng, 2007].

## A2. Inverse Methodology

[23] In our work, we retrieve atmospheric and surface properties through a rigorous inversion of the TES spectra based on an optimal estimation algorithm similar to that developed by AER for the Cross-track Infrared Sounder (CrIS) on the National Polar-Orbiting Environmental Satellite System (NPOESS) [Moncet *et al.*, 2001]. This algorithm has been adapted to Mars to perform self-consistent atmospheric corrections necessary to retrieve accurate values of surface emissivities. Our inversion methodology is based on a constrained nonlinear least squares approach [Rodgers, 1976], in which the solution is found by minimizing a cost function of the form

$$\phi(x) = \|y_o - F(x)\|^2 + g(x) \quad (\text{A2})$$

where the first term is the error associated with the unconstrained solution and the second term is the penalty function that is used to constrain the solution. The state vector  $x$  represents the atmospheric and surface parameters to be retrieved, which in this case include temperature profiles, dust opacities, surface temperature, and surface emissivities. The vectors  $y_o$  and  $F(x)$  represent the observed radiances and radiances calculated using the OSS atmospheric forward model, respectively. If both the state vector and the radiances are characterized by Gaussian distributions, then the cost function has the form

$$\phi(x) = [y_o - F(x)]^T S_\varepsilon^{-1} [y_o - F(x)] + (x - x_{\text{prior}})^T S_{\text{prior}}^{-1} (x - x_{\text{prior}}) \quad (\text{A3})$$

where  $S_\varepsilon$  is an error covariance matrix describing the measurement and other errors and  $x_{\text{prior}}$  and  $S_{\text{prior}}$  are the background (a priori) vector and the associated error covariance matrix, respectively. An iterative solution to the inverse problem can be obtained by minimizing this cost function via a Gauss-Newton method. When the second derivative of  $F(x)$  is neglected, the solution  $x_{i+1}$  at the  $(i + 1)$ th iteration, given the solution  $x_i$  at the  $i$ th iteration, is equal to

$$x_{i+1} = x_{\text{prior}} + \left( K_i^T S_\varepsilon^{-1} K_i + S_{\text{prior}}^{-1} \right)^{-1} \cdot K_i^T S_\varepsilon^{-1} [y_o - y_i + K_i (x_i - x_{\text{prior}})] \quad (\text{A4})$$

where  $y_i$  is the current value of  $F(x)$  linearized about  $x_{\text{prior}}$  and  $K_i$  is the Jacobian matrix containing partial derivatives of  $y_i$  with respect to  $x$ .

[24] Given the lack of direct surface pressure measurements, surface pressure is set equal to the values available in the PDS (estimated from topography and GCM data). We note that the optimal estimation method offers a natural mechanism for quantifying the impact of this and other uncertainties on the retrieved products (e.g., lack of sensitivity to the surface under very dusty conditions will be reflected in the a posteriori error covariance matrix). The need for an a priori constraint relates to the fact that the inversion problem is generally ill conditioned. The use of a

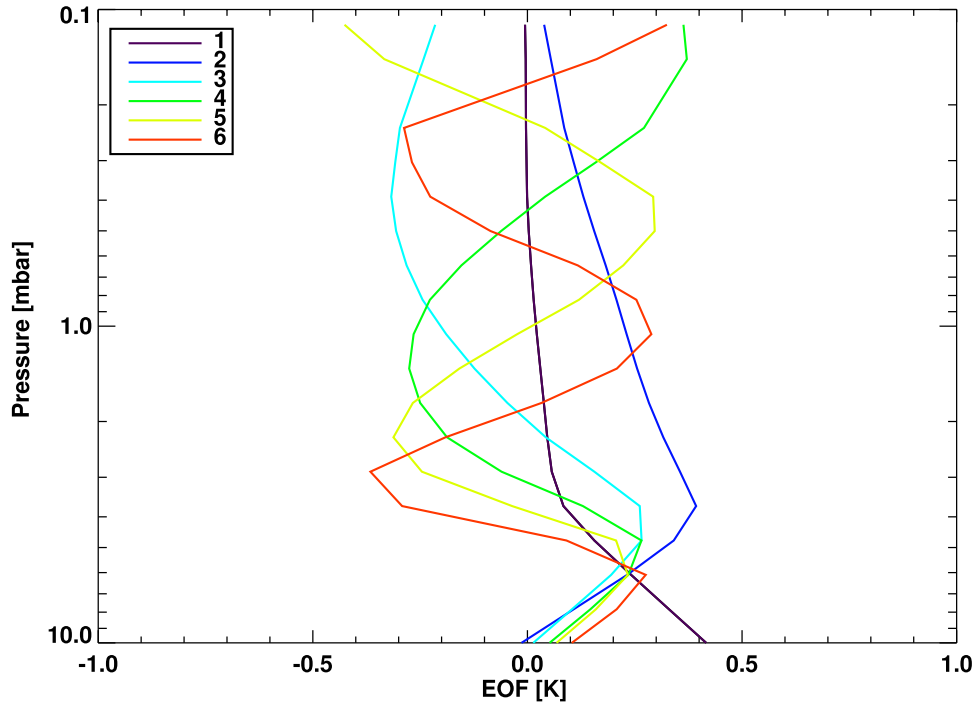


**Figure A1.** The first six EOFs of the a priori covariance matrix  $S_{\text{prior}}$  for atmospheric temperature used in the retrievals described in this paper.

priori information constrains the derived solution to physically acceptable solution. However, the background covariance introduces interlevel correlation in the retrieved temperature profiles (to prevent the solution from being unstable) and if the constraint is biased, it will introduce errors into the solution. In the work described in this paper, the atmospheric covariance is derived from an ensemble profiles generated in the Mars GCM [Wilson and Hamilton, 1996]. In order to minimize the a priori constraint, these profiles have been taken from the nonpolar regions, with the a priori atmospheric temperature profile set to the mean of these profiles.

[25] For parameters without complete statistical a priori information, e.g., dust opacities and surface emissivities at discrete frequencies, no correlations are included in the a priori covariance matrix. It should be noted that while, in general, the relatively large number of TES channels is expected to provide enough information for the solution to be not overly dependent on the a priori statistics, this does not apply to the cold polar regions, where a realistic a priori on surface emissivity is essential for a realistic retrieval of surface temperature (see section 3).

[26] As is typical in infrared inversion problems, the solution is unstable (or impossible to achieve) when the retrieval is attempted for all elements of the state vector used in the forward model (i.e., 21 levels of the atmospheric temperature profile in this case). To circumvent this problem, we project the temperature profiles onto a set of precomputed empirical orthogonal functions (EOFs) obtained by applying a principal component analysis to the error covariance matrix  $S_{\text{prior}}$  (computed from the deviations from the mean profile). The first six EOFs are shown in Figure A1. The iterative solution given by equation (A4) is not changed by the EOF transformation. Before the inver-

sion,  $\Delta x \equiv x_{i+1} - x_{\text{prior}}$  and  $K_i$  are transformed into the EOF domain according to the following equations

$$\Delta \tilde{x} = U^T \Delta x \quad (\text{A5})$$

$$\tilde{K}_i = K_i U \quad (\text{A6})$$

where  $U$  is the matrix that contains only the selected significant EOFs. In the retrieval shown in this paper, only the first three EOFs have been used, thus reducing the dimensionality of the problem and stabilizing the solution. Sensitivity studies have shown that employing six EOFs changes the results only slightly, while with a significantly larger number of EOFs, no stable solution can be found. The diagonalization of  $S_{\text{prior}}$  is given by

$$\Lambda = U^T S_{\text{prior}} U \quad (\text{A7})$$

and the transformed retrieval equation reads

$$\Delta \tilde{x}_{i+1} = (\tilde{K}_i^T S_e^{-1} \tilde{K}_i + \Lambda^{-1})^{-1} \tilde{K}_i^T S_e^{-1} (y_o - y_i + \tilde{K}_i \Delta \tilde{x}_i) \quad (\text{A8})$$

[27] **Acknowledgments.** This work has been supported by the NASA Mars Fundamental Research and Mars Data Analysis Programs. We thank the reviewers for improving the paper, particularly Timothy Titus for pointing out the importance of the zero-radiance-level correction and applying it to the spectra used in our retrievals.

## References

Banfield, D., B. J. Conrath, M. D. Smith, P. Christensen, and R. J. Wilson (2003), Forced waves in the Martian atmosphere from MGS TES nadir data, *Icarus*, *161*, 319–345, doi:10.1016/S0019-1035(02)00044-1.

- Banfield, D., B. J. Conrath, P. J. Gierasch, R. J. Wilson, and M. D. Smith (2004), Traveling waves in the Martian atmosphere from MGS TES nadir data, *Icarus*, *170*, 365–403, doi:10.1016/j.icarus.2004.03.015.
- Christensen, P. R. (2002), MGS M Thermal Emission Spectrometer 3 TSDR V2.0, MGS-M-TES-3-TSDR-V2.0, <http://starbrite.jpl.nasa.gov/pds/viewProfile.jsp?dsid=MGS-M-TES-3-TSDR-V2.0>, Planet. Data Syst., Washington, D. C.
- Christensen, P. R., et al. (2001), Mars Global Surveyor Thermal Emission Spectrometer experiment: Investigation description and surface science results, *J. Geophys. Res.*, *106*, 23,823–23,871, doi:10.1029/2000JE001370.
- Clough, S. A., M. J. Iacono, and J.-L. Moncet (1992), Line-by-line calculation of atmospheric fluxes and cooling rates: Application to water vapor, *J. Geophys. Res.*, *97*, 15,761–15,785.
- Clough, S. A., M. J. Iacono, D. D. Turner, T. R. Shippert, J. C. Liljgren, D. C. Tobin, H. E. Revercomb, and R. O. Knuteson (1999), Effect on the calculated spectral surface radiances due to MWR scaling of sonde water vapor profiles, paper presented at Ninth ARM Science Team Meeting, Dep. of Energy, Washington, D. C. (Available online at <http://www.arm.gov/publications/proceedings/conf09/abstracts/clough-99.pdf>)
- Clough, S. A., M. W. Shephard, E. J. Mlawer, J. S. Delamere, M. J. Iacono, K. Cady-Pereira, S. Boukabara, and P. D. Brown (2005), Atmospheric radiative transfer modeling: A summary of the AER codes, short communication, *J. Quant. Spectrosc. Radiat. Transfer*, *91*, 233–244, doi:10.1016/j.jqsrt.2004.05.058.
- Clough, S. A., M. W. Shephard, and V. H. Payne (2008), Implications for molecular spectroscopy inferred from IASI satellite spectral measurements, paper presented at Tenth Biennial HITRAN Conference, Air Force Cambridge Res. Lab., Bedford, Mass.
- Colaprete, A., J. R. Barnes, R. M. Haberle, J. L. Hollingsworth, H. H. Kieffer, and T. N. Titus (2005), Albedo of the south pole on Mars determined by topographic forcing of atmosphere dynamics, *Nature*, *435*, 184–188, doi:10.1038/nature03561.
- Colaprete, A., J. R. Barnes, R. M. Haberle, and F. Montmessin (2008), CO<sub>2</sub> clouds, CAPE and convection on Mars: Observations and general circulation modeling, *Planet. Space Sci.*, *56*, 150–180.
- Conrath, B. J., J. C. Pearl, M. D. Smith, W. C. Maguire, S. Dason, M. S. Kaelberer, and P. R. Christensen (2000), Mars Global Surveyor Thermal Emission Spectrometer (TES) observations: Atmospheric temperatures during aerobraking and science phasing, *J. Geophys. Res.*, *105*, 9509–9519, doi:10.1029/1999JE001095.
- Eluszkiewicz, J. (2005), On the microphysical state of the Martian seasonal caps, *Icarus*, *103*, 43–48, doi:10.1006/icar.1993.1056.
- Eluszkiewicz, J., J.-L. Moncet, T. N. Titus, and G. B. Hansen (2005a), A microphysically based approach to modeling emissivity and albedo of the Martian seasonal caps, *Icarus*, *174*, 524–534, doi:10.1016/j.icarus.2004.05.025.
- Eluszkiewicz, J., K. Cady-Pereira, G. Uymin, and J.-L. Moncet (2005b), Martian radiative transfer modeling using the Optimal Spectral Sampling method, *Lunar Planet. Sci.*, XXXVI, Abstract 2181.
- Hansen, G. B. (1997), The infrared absorption spectrum of carbon dioxide ice from 1.8 to 333  $\mu\text{m}$ , *J. Geophys. Res.*, *102*, 21,569–21,587, doi:10.1029/97JE01875.
- Ivanov, A. B., and D. O. Muhleman (2001), Cloud reflection observations: Results from the Mars Orbiter Laser Altimeter, *Icarus*, *154*, 190–206, doi:10.1006/icar.2001.6686.
- Kieffer, H. H., T. N. Titus, K. F. Mullins, and P. R. Christensen (2000), Mars south polar spring and summer behavior observed by TES: Seasonal cap evolution controlled by frost grain size, *J. Geophys. Res.*, *105*, 9653–9699, doi:10.1029/1999JE001136.
- Langevin, Y., S. Douté, M. Vincendon, F. Poulet, J.-P. Bibring, B. Gondet, B. Schmitt, and F. Forget (2006), No signature of clear CO<sub>2</sub> ice from the ‘cryptic’ regions in Mars’ south seasonal polar cap, *Nature*, *442*, 790–792, doi:10.1038/nature05012.
- Moncet, J.-L., et al. (2001), Algorithm theoretical basis document for the Cross-track Infrared Sounder (Cris) Environmental Data Records (EDR), *Rep. P882-TR-E-1.2.3-ATBD-03-01*, Atmos. Environ. Res., Inc., Lexington, Mass. (Available at [http://eic.ipc.noaa.gov/IPOarchive/SCI/atbd/cris\\_atbd\\_03\\_09\\_01.pdf](http://eic.ipc.noaa.gov/IPOarchive/SCI/atbd/cris_atbd_03_09_01.pdf))
- Moncet, J.-L., G. Uymin, A. E. Lipton, and H. E. Snell (2008), Radiance modeling at high spectral resolution by optimal spectral sampling, *J. Atmos. Sci.*, in press.
- Niro, F., K. Jucks, and J.-M. Hartmann (2005), Spectral calculations in central and wing regions of CO<sub>2</sub> IR bands: IV. Software and database for the computation of atmospheric spectra, *J. Quant. Spectrosc. Radiat. Transfer*, *95*, 469–481.
- Pettengill, G. H., and P. G. Ford (2000), Winter clouds over the north Martian polar cap, *Geophys. Res. Lett.*, *27*, 609–612, doi:10.1029/1999GL010896.
- Richardson, M. I., and R. J. Wilson (2002), Investigation of the nature and stability of the Martian seasonal water cycle with a general circulation model, *J. Geophys. Res.*, *107*(E5), 5031, doi:10.1029/2001JE001536.
- Rodgers, C. D. (1976), Retrieval of atmospheric temperature and composition from remote measurements of thermal radiation, *Rev. Geophys.*, *14*, 609–624, doi:10.1029/RG014i004p00609.
- Rodgers, C. D. (2000), *Inverse Methods for Atmospheric Sounding: Theory and Practice*, World Sci., Hackensack, N. J.
- Saunders, R., et al. (2007), A comparison of radiative transfer models for simulating Atmospheric Infrared Sounder (AIRS) radiances, *J. Geophys. Res.*, *112*, D01S90, doi:10.1029/2006JD007088.
- Smith, M. D. (2002), The annual cycle of water vapor on Mars as observed by the Thermal Emission Spectrometer, *J. Geophys. Res.*, *107*(E11), 5115, doi:10.1029/2001JE001522.
- Smith, M. D. (2004), Interannual variability in TES Atmospheric observations of Mars during 1999–2003, *Icarus*, *167*, 148–165, doi:10.1016/j.icarus.2003.09.010.
- Smith, M. D., J. C. Pearl, B. J. Conrath, and P. R. Christensen (2000), Mars Global Surveyor Thermal Emission Spectrometer (TES) observations of dust opacity during aerobraking and science phasing, *J. Geophys. Res.*, *105*, 9539–9552, doi:10.1029/1999JE001097.
- Titus, T. N., H. H. Kieffer, K. F. Mullins, and P. R. Christensen (2001), TES remapping data: Slab ice and snow flurries in the Martian north polar night, *J. Geophys. Res.*, *106*, 23,181–23,196, doi:10.1029/2000JE001284.
- Turner, D. D., et al. (2004), The QME AERI LBLRTM: A closure experiment for downwelling high spectral resolution infrared radiance, *J. Atmos. Sci.*, *61*, 2657–2675, doi:10.1175/JAS3300.1.
- Wang, H., M. I. Richardson, R. J. Wilson, A. P. Ingersoll, A. D. Toigo, and R. W. Zurek (2003), Cyclones, tides and the origin of a cross-equatorial dust storm on Mars, *Geophys. Res. Lett.*, *30*(9), 1488, doi:10.1029/2002GL016828.
- Wang, H., R. W. Zurek, and M. I. Richardson (2005), The relationship between frontal dust storms and transient eddy activity in the northern hemisphere of Mars as observed by Mars Global Surveyor, *J. Geophys. Res.*, *110*, E07005, doi:10.1029/2005JE002423.
- Weng, F. (2007), Advances in radiative transfer modeling in support of satellite data assimilation, *J. Atmos. Sci.*, *64*, 3799–3807, doi:10.1175/2007JAS2112.1.
- Wilson, R. J. (2000), Evidence for diurnal period Kelvin waves in the Martian atmosphere from Mars Global Surveyor TES data, *Geophys. Res. Lett.*, *27*, 3889–3892, doi:10.1029/2000GL012028.
- Wilson, R. J., and K. P. Hamilton (1996), Comprehensive model simulation of thermal tides in the Martian atmosphere, *J. Atmos. Sci.*, *53*, 1290–1326, doi:10.1175/1520-0469(1996)053<1290:CMSOTT>2.0.CO;2.
- Wilson, R. J., D. Banfield, B. J. Conrath, and M. D. Smith (2002), Traveling waves in the northern hemisphere of Mars, *Geophys. Res. Lett.*, *29*(14), 1684, doi:10.1029/2002GL014866.
- Wiscombe, W. J., and J. W. Evans (1977), Exponential-sum fitting of radiative transmission functions, *J. Comput. Phys.*, *24*, 416–444, doi:10.1016/0021-9991(77)90031-6.
- Wolff, M. J., and R. T. Clancy (2003), Constraints on the size of Martian aerosols from Thermal Emission Spectrometer observations, *J. Geophys. Res.*, *108*(E9), 5097, doi:10.1029/2003JE002057.

K. Cady-Pereira, T. Connor, J. Eluszkiewicz, J.-L. Moncet, M. W. Shephard, and G. Uymin, Atmospheric and Environmental Research, Inc., 131 Hartwell Avenue, Lexington, MA 02421, USA. (jel@aer.com)